Femoral strength and strains in sideways fall: Validation of finite element models against bilateral strain measurements

Joeri Kok *, Lorenzo Grassi, Anna Gustafsson, Hanna Isaksson

Department of Biomedical Engineering, Lund University, Sweden

ARTICLE INFO

ABSTRACT

Low impact falls to the side are the main cause of hip fractures in elderly. Finite element (FE) models of the proximal femur may help in the assessment of patients at high risk for a hip fracture. However, extensive validation is essential before these models can be used in a clinical setting. This study aims to use strain measurements from bilateral digital image correlation to validate an FE model against ex vivo experimental data of proximal femora under a sideways fall loading condition. For twelve subjects, full-field strain measurements were available on the medial and lateral side of the femoral neck. In this study, subject-specific FE models were generated based on a consolidated procedure previously validated for stance loading. The material description included strain rate dependency and separate yield and fracture strain limits in tension and compression. FE predicted fracture force and experimentally measured peak forces showed a strong correlation ($R^2 = 0.92$). The FE simulations predicted the fracture initiation within 3 mm distance of the experimental fracture line for 8/12 subjects. The predicted and measured strains correlated well on both the medial side ($R^2 = 0.87$) and the lateral side ($R^2 = 0.74$). The lower correlation on the lateral side is attributed to the irregularity of the cortex and presence of vessel holes in this region. The combined validation against bilateral full-field strain measurements and peak forces has opened the door for a more elaborate qualitative and quantitative validation of FE models of femora under sideways fall loading.

1. Introduction

Hip fractures are a large and growing socio-economic burden in the western society, with incidences for countries in the EU ranging from 231/100,000 (Romania) to 640/100,000 (Denmark) for people over the age of 50 alone (Hernlund et al., 2013). Costs directly related to these fractures have been estimated to be around €20 billion for the EU in 2010 (Hernlund et al., 2013). Hip fractures can mostly be attributed to low bone strength and a low-impact fall to the side (Parkkari et al., 1999). Current diagnostics of osteoporosis and assessment of fracture risk rely on measurements of the areal bone mineral density (aBMD) from 2D dual energy x-ray absorptiometry images. These scans are relatively cheap and fast but around 3/4 of people with a low-impact hip fracture are not assessed to be at high risk by aBMD alone (Pasco et al., 2006). By using quantitative computed tomography (QCT), subject-specific 3D finite element (FE) models can be created and used to predict the mechanical behavior of the proximal femur during a fall (Johannesdottir et al., 2018). Fracture force as predicted by FE models is likely a better predictor for fracture risk than aBMD (Orwoll et al., 2009). However, these models are currently not widely accepted as a clinical tool for the prediction of fracture risk. This is partly due to the lack of accurate quantitative validation of FE models predicting the fracture behavior of the proximal femur.

Fracture strength is the parameter most used for validation and most relevant for clinical use (Johannesdottir et al., 2017; Viceconti et al., 2018). Multiple studies have shown strong correlations between experimentally measured forces and fracture forces predicted by FE models (Dall'Ara et al., 2013; Enns-Bray et al., 2018; Keyak et al., 2005; Koivumäki et al., 2012; Zysset et al., 2013). However, due to a large variation in experimental setups and FE modeling approaches there is no consensus on which FE models best represent the full mechanical behavior of the femur when loaded. For further validation of FE models, additional measurements are required. Strain measurements using strain gauges are often used (Grassi et al., 2012; Helgason et al., 2016). Although measurements with strain gauges have a high temporal accuracy, only a limited number can be placed on a bone. This typically

* Corresponding author at: Department of Biomedical Engineering, Lund University, Box 118, 221 00 Lund, Sweden.
  E-mail address: joeri.kok@bme.lth.se (J. Kok).

results in a low spatial resolution with no more than 15 prese-lected measurement points (Grassi and Isaksson, 2015).

A promising approach for validation of FE models of femora that enables full-field strain measurements on the surface of the bone is digital image correlation (DIC) (Gilchrist et al., 2013). In recent studies, FE models of the proximal femur were validated using a 3D-surface DIC setup (Grassi et al., 2016; Katz and Yosibash, 2020). Linear regression between strains measured with DIC and strains predicted by FE-analysis correlated strongly in these studies. However, they investigated the single-leg-stance loading condition, which is clinically less relevant than sideways falls (Parkkari et al., 1999). Helgason et al. (2014) performed a validation of an FE model simulating a sideways fall loading condition by comparing the model to experimental DIC measurements. However, in this case, only one femur and a 2D DIC setup was used, which limits the possibility to quantitatively analyze the strains. Recently, experimental strain measurements on 12 femora under sideways fall loading have been obtained with a 3D DIC setup in our group (Grassi et al., 2020).

This study aims to use ex vivo bilateral strain measurements on proximal femora under a sideways fall loading condition to validate an FE model. The FE modeling approach includes strain-rate dependency and yield and failure limits for bone. This approach has previously been validated for a stance loading condition (Grassi et al., 2016). Additionally, predicted fracture strength and observed fracture location are compared to the experimental results.

2. Methods

2.1. Experimental mechanical testing

The experimental data was reported in detail in Grassi et al. (2020) and is used in this study for comparison. Briefly, twelve human female cadaver proximal femora were harvested fresh at Kuopio University Hospital, Finland (ethical permission 5783/2004/044/07). None of the donors had any reported musculoskeletal disorder. Details on donor height (range: 1.53–1.74 m), weight (48–120 kg), age (22–88 years), and femoral neck aBMD (0.429–1.053 g/cm^2) can be found in Grassi et al. (2020). The specimens were scanned before the experiment using QCT while contained in ice (Definition AS64, Siemens AG, voxel size of 0.4 × 0.4 × 0.6 mm, 120 kVp, 210 mAs) with a hydroxyapatite calibration phantom (QRM-BDC/6, Quality Assurance in Radiology and Medicine). Additionally, μCT images were taken in air both before (Nikon XT H 225 scanner, isotropic voxel size of 52–60 μm, 100 kVp, 0.2 mA) and after the experiment (MILabs U-CT system, isotropic voxel size of 60 μm, 65 kVp, 0.13 mA).

The twelve femora were mechanically tested to failure in a sideways fall configuration (10° adduction, 15° internal rotation, 5 mm/s until macroscopic failure, for details please see Grassi et al. (2020), and strains were measured using DIC on the medial and lateral surface of the femoral neck (Fig. 1a). Two cameras on the medial side recorded images at 6400 fps (1024 × 1024 pixels, ~20 pixels/mm) and two cameras on the lateral side recorded images at 500 fps (1280 × 1024 pixels, ~18 pixels/mm). DIC was performed on the acquired images and the engineering strains were retrieved at each frame with a data point density of approximately 5 points/mm^2 (medial) and 13 points/mm^2 (lateral).

2.2. Finite element modeling

FE models were generated following an established procedure (Grassi et al., 2016). The femur geometry was semi-automatically segmented from the CT images by thresholding at an apparent mineral density (ρ_{app}) of ~ 100 mg/cm^3 and manual correction (Seg3D2, University of Utah). The segmented triangulated geometries were used to create a smooth surface model consisting of B-spline surfaces (Autodesk Meshmixer 3.4.45, Autodesk, Solidworks 2018, Dassault Systèmes). This surface model was then converted to a second-order tetrahedral mesh with element sizes of ~ 1 mm between the minor trochanter and the epoxy on the femoral head and major trochanter and ~ 3 mm for the rest (Hypermesh v17.0, Altair Engineering) (Fig. 1b). A mesh sensitivity analysis similar to the one presented in Helgason et al. (2008) was performed (Supplementary Fig. 1). Changes in predicted fracture force and total strain energy density remained below 1% when further increasing the number of elements.

For each element in the femur, ρ_{app} in g/cm^3 was derived from the QCT scans (Bonemat_V3 (Taddei et al., 2007)). A constant Young's modulus (E_0) in MPa was then calculated for each element using the density-elasticity relationship: $E_0 = 6850 * \rho_{app}^{1.49}$ (Morgan et al., 2003). All elements at the surface of the mesh were assigned a minimum Young's modulus of 2.5 GPa. The Poisson's ratio was set to 0.4 (Reilly and Burstein, 1975). The elements in the embedding material around the femur (epoxy, Technovit 4071, Heraeus Kulzer) were assigned an isotropic Young's modulus of 2.5 GPa. The geometry of the distal epoxy pot was used to identify the experimental reference system and to assign the appropriate boundary conditions (Fig. 1b). FE-simulations were performed in Abaqus (v2017, Dassault Systèmes).

The material model of the bone included strain rate dependency with different strain limit values for yield and failure under compression (minor principal strains) and tension (major principal strains), as earlier described by Grassi et al. (2016). The strain rate dependency and strain limits were based on the average principal
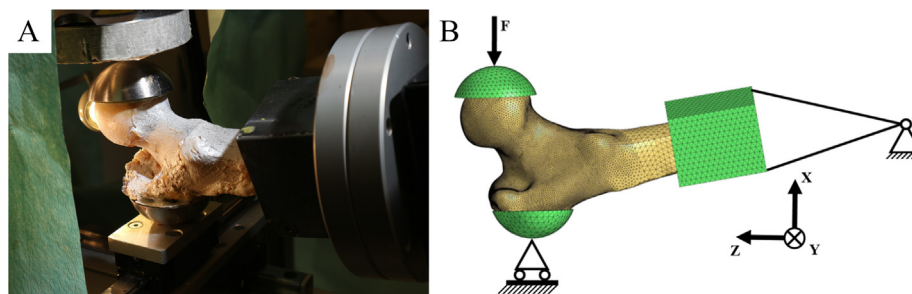

Fig. 1. A) A femur prepared and mounted in the loading device for the experimental mechanical testing (see Grassi et al. 2020 for details). B) A graphical representation of the loading conditions on the FE model. The epoxy around the distal end was aligned with the coordinate system and then rotated 15° around the z-axis (internal rotation) and 10° around the y-axis (adduction). The load was equally distributed among the most medial surface node and the surface nodes connected to this node on the epoxy cup on the femoral head. The most lateral surface node and the surface nodes connected to this node on the epoxy cup were constrained in the x-direction. All surface nodes except those on the proximal side of the epoxy pot were connected to a node that only allows rotation around the y-axis.

strains for all elements within a 3 mm radius of the element. Each element was assigned its specific initial modulus (E_0) as described above. If the strain rate of an element exceeded the reference strain rate (SR_{ref}) of 0.5%/s (Bayraktar et al., 2004) the elastic modulus of the element was adjusted using the strain rate correction factor: $SRCF = (SR_{elem}/SR_{ref})^{0.06}$, where SR_{elem} is the absolute maximum principal strain rate. This correction factor is based on the dependency of a bones' stiffness on the strain rate (Carter and Hayes, 1977, 1976). The tangent modulus was then defined as: $E_{new} = SRCF * E_0$. When element strain exceeded the yield strain limit (1.04% compression, 0.73% tension (Bayraktar et al., 2004)), the modulus was reduced to 5.5% of the tangent modulus (Reilly et al., 1974), and the simulation continued. A femur was considered failed when the ultimate strain limit (2.11% compression, 2.74% tension (Reilly et al., 1974)) was exceeded for any of the elements on the surface of the femur. The force when the first element failed was taken as the predicted fracture force. The FE-analyses were conducted by applying consecutive 0.05 mm increments with the time increment tuned to a 5 mm/s displacement rate.

2.3. Data analysis

2.3.1. Fracture force prediction

Linear regression analysis between the predicted and measured fracture forces was performed to assess the fracture force prediction accuracy of the FE models. From the regression the coefficient of determination and standard error of the estimate (SEE) were determined.

2.3.2. Fracture onset location

The fracture onset locations predicted by the FE models were compared to the fracture line resulting from the experiment. The µCT scans of the broken bones were registered to the FE models (CloudCompare v2.8.1, www.cloudcompare.org/), and the shortest distance between the predicted fracture initiation and the fracture line following from the mechanical loading was measured. The FE predicted fracture locations were also compared to the µCT images of the intact bone to identify the structure of the bone underlying the predicted fracture location.

2.3.3. Strain prediction

Strain prediction accuracy was evaluated at a force representing 90% of the experimentally measured peak force. The principal strains calculated by the FE models were compared to DIC measurements. The points from the DIC measurements were registered onto the surfaces of the FE models using an iterative closest point approach (CloudCompare v2.8.1). The size of the DIC point cloud was reduced before the comparison with the strains predicted by the FE models by removing the two outermost layers of points, as strain measurements at the edge of the region are often less accurate (Grassi et al., 2016; Katz and Yosibash, 2020). For experimentally measured points a confidence interval (σ) was calculated (Vic-3D v7, Correlated Solutions, Inc.), as a measure for how accurately the displacement of each point is calculated between subsequent images (Sutton et al., 2009). Points where σ exceeded 0.02 pixels were excluded before correlation.

A data comparison method was adopted, based on our previous procedure (Grassi et al., 2016, 2013). For each element on the surface of the mesh, the smallest sphere circumscribing it was calculated. All DIC strain measurement points within the sphere were averaged, and the obtained value compared to the FE element strain. Robust linear regression analysis was performed to assess the correlation between the predicted and measured major and minor principal strains.

For one subject (CAD052) a technical error occurred leading to the inability to connect the DIC measurements to the correct load. On another subject (CAD060) severe leakage of bone marrow on the lateral side at 90% of the peak force resulted in a σ over 0.02 for all DIC measurements. Thus, the strains on the medial and lateral side were correlated for 11 and 10 subjects, respectively.

3. Results

3.1. Fracture force prediction

The fracture forces predicted by the FE model ranged from 1.71 to 5.00 kN and correlated well with the peak forces measured in the experiment (R^2 = 0.92, SEE = 0.44 kN). The predicted forces were slightly overestimated for the weaker bones and underestimated for the stronger bones leading to an intercept above 0 and a slope below 1 (Fig. 2).

3.2. Fracture onset location

The FE models predicted that the fractures initiate under compression on the lateral side of the femoral neck (Fig. 3). Similarly, in the experiment, compressive damage on the lateral side, mostly
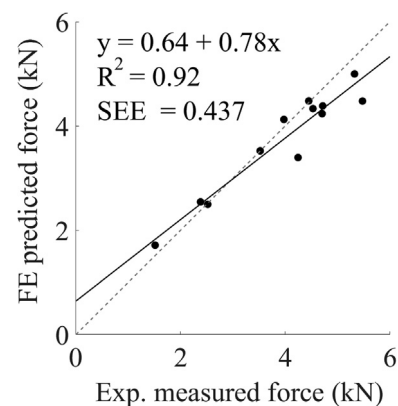

Fig. 2. Linear regression plot, showing the correlation between the experimentally measured peak force and the fracture force predicted by FE-analysis.
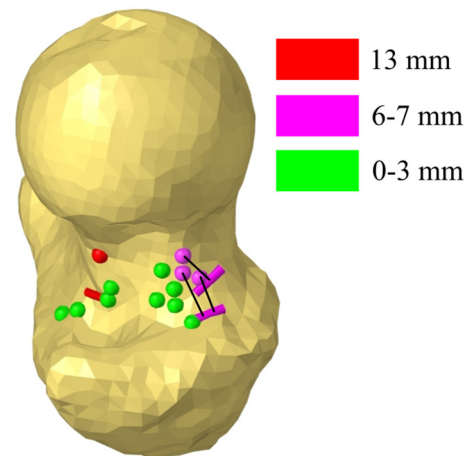

Fig. 3. The distances (mm) measured between predicted fracture locations (spheres) and the fracture lines (bars, only shown for distances > 3 mm) as determined from µCT scans taken after the experiment. The black lines indicate which predicted fracture location relates to which fracture line.
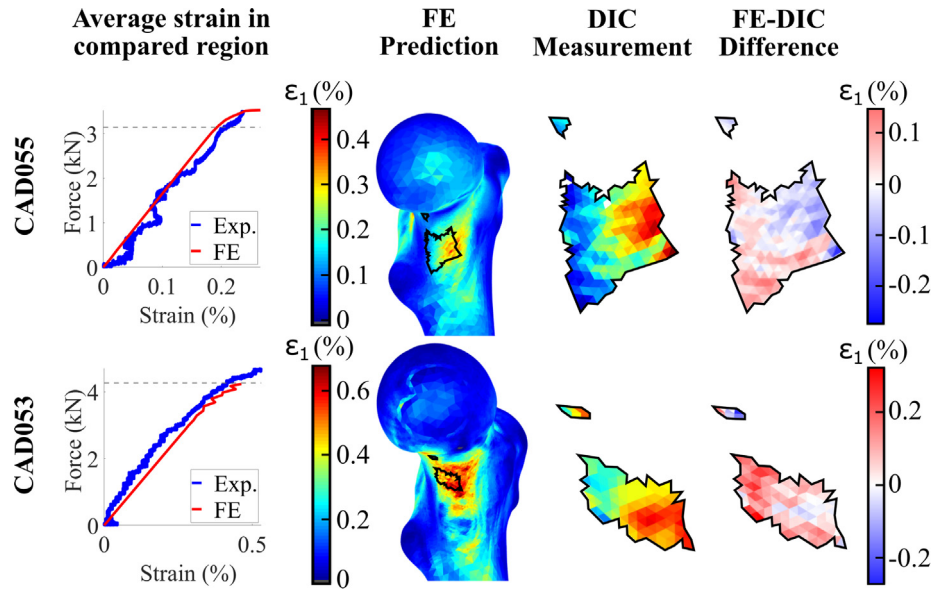
Fig. 4. Left) Plots of the force against the average measured major principal strain (ε_1) for all DIC points and elements in the compared region on the medial side. The represented subjects are those with the highest (CAD055) and lowest (CAD053) correlation coefficient between the predicted and measured strains on this side at 90% of the measured peak force (indicated by the dotted line). The plots are cropped at the maximum measured and predicted force. Right) Maps of the major principal strains (ε_1) on the medial side at 90% peak force. The scalebars are adjusted to the minimum and maximum values in their respective plots.

due to crushing of the trochanteric region, was observed as the main cause for a force drop after reaching the peak force (Grassi et al., 2020). Most (8/12) predicted fracture locations were within 3 mm of the actual fracture line. The less accurately predicted fracture locations were all more proximal on the neck. Comparisons with the µCT images showed that the fractures were predicted in or near a vessel hole (5/12), in a region with high cortical porosity (5/12), or somewhere else on the superolateral aspect of the femoral neck, without clear underlying cause (2/12) (Supplementary Fig. 2).

3.3. Strain prediction

Plots of the force against the average strain in the measured region show a good global agreement between the predicted and measured mechanical behavior, especially in the elastic region (Figs. 4 and 5). The region with the highest predicted tensile strains is captured within the DIC region on the medial side (Fig. 4), whereas the highest predicted compressive strains are not included in the available DIC measurements on the lateral side (Fig. 5).
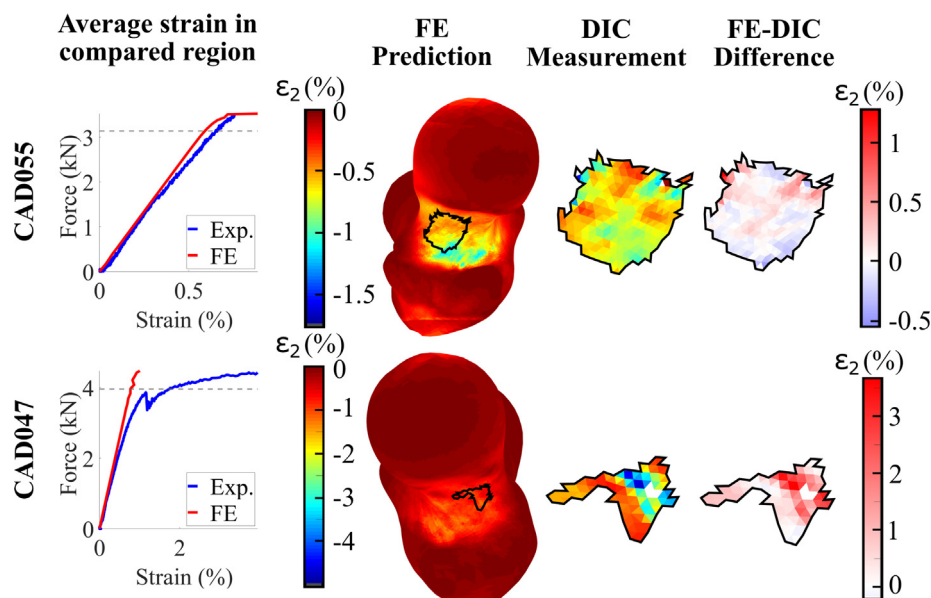

Fig. 5. Left) Plots of the force against the average measured absolute minor principal strain (ε_2) for all DIC points and elements in the compared region on the lateral side. The represented subjects are those with the highest (CAD055) and lowest (CAD047) correlation coefficient between the predicted and measured strains on this side at 90% of the measured peak force (indicated by the dotted line). The plots are cropped at the maximum measured and predicted force. Right) Maps of the minor principal strains (ε_2) on the lateral side at 90% peak force for these subjects. The scalebars are adjusted to the minimum and maximum values in their respective plots.
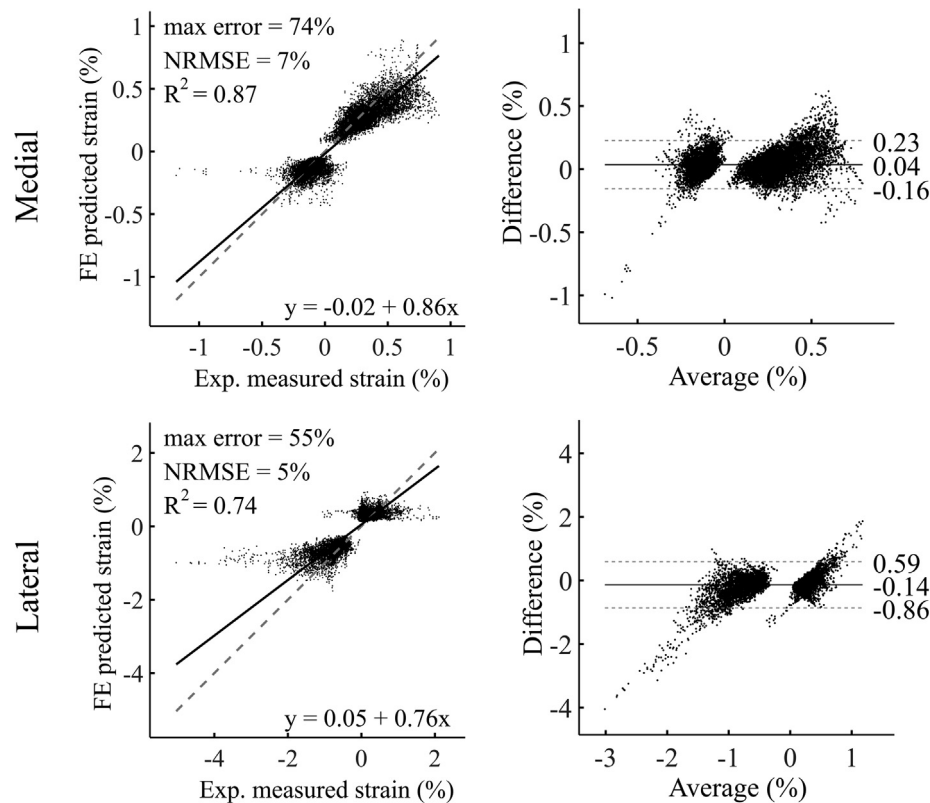
Fig. 6. Left) Results from the robust linear regression between FE predicted and experimentally measured principal strains for all subjects pooled. Right) Bland-Altman plots showing the agreement between predicted and measured strains for all bones pooled. The solid line represents the mean difference and the dotted lines ± 1.96*SD.

For all bones pooled, the FE predicted major and minor principal strains correlated well with the experimentally measured major and minor principal strains on the medial side (Fig. 6). The Bland-Altman plots show that the mean difference between the strains was 0.04% with a ± 1.96*SD of −0.16% – 0.23%. This indicates that strains predicted by the FE models are in relatively good agreement with the experimental measurements, as the FE predicted strains on the lateral side show a weaker correlation and a worse agreement (mean difference: −0.13; ±1.96*SD: −0.84 – 0.58). For the individual subjects, the strains on the medial side

correlated consistently well between FE models and experimental data (R^2 range: 0.82–0.96; slopes: 0.75–1.39; intercepts: −0.06% – 0.02%) (Supplementary Fig. 3). On the lateral side, the range between the samples was higher and the strains correlated less well in some samples (R^2 range: 0.67–0.98; slopes: 0.36 –1.58; intercepts: −0.11% – .29%).

In some cases, the region with the DIC measurements on the lateral side included vessel holes leading to relatively high experimentally measured strains (Fig. 7). Although the FE predicted fracture location was often close to a vessel hole, the FE models did not
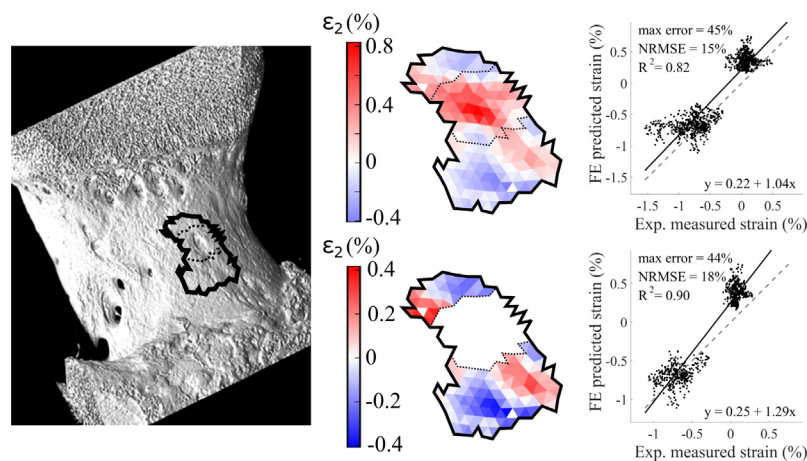

Fig. 7. Effect of the vessel holes on the correlation between predicted and measured strains in the lateral neck. Left) A segmentation of the lateral neck with the region used for the DIC measurement outlined. Middle) The plots showing the difference in predicted and measured minor principal strains including (top) and excluding (bottom) the region around the vessel hole. Right) The correlations between predicted and measured strains including (top) and excluding (bottom) the region around the vessel hole.

predict strains around vessel holes as high as the experimental measurements. For the subject shown in Fig. 7, a stronger correlation (R^2 increase from 0.82 to 0.90) between FE predicted and experimentally measured strains was achieved when the experimentally measured data in the vicinity of the vessel hole was excluded. A similar improvement could be seen in the mean difference (increase from −0.20% with a ± 1.96*SD of −0.65% – 0.24% to −0.16% with a ± 1.96*SD of −0.58%–0.25%).

4. Discussion

The aim of this study was to use ex vivo bilateral strain measurements on proximal femora under a sideways fall loading condition to validate an FE modeling approach.

The fracture force predicted by the FE models correlated well with the measured peak forces. With an R^2 of 0.92, it is higher than what has been reported previously in other studies where similar loading conditions were investigated: R^2 = 0.87 (Koivumäki et al., 2012) and R^2 = 0.85 (Dall'Ara et al., 2013). Furthermore, the SEE in these studies was similar (0.44 kN in both the current study and in Dall'Ara et al. (2013) and 0.39 kN in Koivumäki et al. (2012)). The FE models in this study overestimated the fracture force for weak bones and underestimated the fracture force for the stronger bones. This effect was also observed by Koivumäki et al. (2012), but not by Dall'Ara et al. (2013) where the fracture force was more consistently overestimated by the FE models.

The FE models consistently predicted the fracture initiation location to be on the lateral side of the femoral neck. Since the fracture onset could not clearly be localized during the experiment, the final fracture line was compared to the predicted fracture location, and the fracture location accuracy calculated as the distance between numerically predicted onset and experimental fracture line. Most of the FE predicted fracture locations (8/12) were predicted within a 3 mm accuracy. In the remaining cases the predicted fracture onset was located more proximally than the true fracture line (Fig. 3). A reason for this could be that failure of trabecular bone and epoxy is currently not considered in the FE models, which may lead to a less accurate representation of, e.g., possible internal collapses occurring around the trochanteric fossa. A comparison between the FE predicted fracture location and μCT images of the bones revealed that the FE predicted fracture onset is found either in weak regions in the cortex or somewhere else on the superolateral aspect of the femoral neck (supplementary Fig. 2). Another numerical study, that used local μFE models, has indicated that vessel holes are potentially involved in primary failure events (Bahaloo et al., 2018). The true magnitude of the strains around these vessel holes and their effect on fracture initiation and development is, however, still unclear and deserves a separate investigation.

The principal strains on the medial side were predicted well by the FE models with an R^2 > 0.8 and a slope > 0.8 for all subjects at 90% of the experimental fracture force. In comparison with the single leg stance loading condition (R^2 > 0.9) the correlations were slightly worse (Grassi et al., 2016). This is expected for three reasons: first, only three samples were tested in single leg stance; second, the sideways fall loading condition is more complex due to the addition of an axis of rotation distally and the freedom of motion at the greater trochanter; third, the shapes of the medial and lateral neck are more irregular than the anterior surface that was measured in Grassi et al. (2016), reducing the accuracy of both the FE models and the experimental measurements. The correlation coefficient can be somewhat inflated when validating pooled minor and major principal strains from DIC measurements. This is because DIC, as compared to the limited data points from SGs, provides thousands of measurements for both strains, while leaving an empty region in the regression plot around zero (since non-deformed areas are typically not measured). Bland-Altman plots were therefore included to better show the agreement between predicted and measured strains (Fig. 6) (Altman and Bland, 1983). They also show that there is some proportional bias in the prediction of the strains. This bias is likely introduced by a difference in maximum local strain between the measured and predicted strain. This means that even if the measured and predicted strains follow the same pattern, the difference between them increases as the average between them increases. Other studies that performed strain validation in a sideways fall loading condition reached correlations with R^2 = 0.90 – 0.91 for 16 pooled models (Helgason et al., 2016) and R^2 = 0.91 for 3 pooled models (Grassi et al., 2012). These studies used the same density-modulus relationship in their FE models as the one presented in this study. However, for the experimental measurements these studies used strain gauges at various locations on the femur. Only one of these was placed on the lateral neck and the FE models overestimated the strains in this region by about 30% (Grassi et al., 2012).

The principal strains on the lateral side were not predicted as well by the FE models. There are several factors contributing to this result. First, the measurements on this side were not as accurate as the measurements on the medial side. The cameras on the lateral side had a lower signal-to-noise ratio and the shape of bone is more irregular on this side, which led to smaller regions that were well illuminated and in focus. Second, in addition to the irregular shape of the femora, the measurements on the lateral side were often influenced by the presence of vessel holes (Grassi et al., 2020). Local damage could occur in these holes leading to high strains not captured by the FE model. Alternatively, these holes could lead to artefacts due to, for example, leakage of bone marrow. In the latter case, the FE model would be expected to describe the mechanical behavior of the bone better. In a similar study, but with a different modeling approach and stance loading condition the results also showed a discrepancy between measured and predicted strains on the lateral neck (Katz and Yosibash, 2020).

The FE modeling approach was previously developed and validated for a single-leg-stance loading condition (Grassi et al., 2016). This means that this modeling approach has now been validated under both a clinically relevant (fall to the side) and a physiologically relevant (single-leg-stance) loading condition. The FE modeling strategy presented in this study differed from the one presented in Grassi et al. (2016) only by the value of the minimum Young's modulus of the elements at the surface (2.5 GPa instead of 5 GPa). This change was implemented because the minimum of 5 GPa was set for relatively young men with a strong cortex. To find an appropriate cortex reinforcement for the subjects in this study (old women), a sensitivity analysis was performed with minimum values of Young's modulus ranging from 0 to 5 GPa. Based on these results (Supplementary Fig. 4), a minimum Young's modulus of 2.5 GPa was selected to correct for errors introduced by partial volume effects without affecting femoral strength (as a 5 GPa did). To increase the robustness of the models and reduce their sensitivity to the mesh size, more accurate mapping of the cortex may be required (Schileo et al., 2020).

In conclusion, bilateral digital image correlation has opened the door for a more elaborate qualitative and quantitative validation of FE models of femora under sideways fall loading. The modeling approach validated in this study could accurately predict the fracture forces and the fracture locations. The novel validation method was used to set a benchmark for validation using high-resolution full-field strain measurements. This validation process highlights the complexity of measured strain fields and difficulties of accurately predicting strains in areas with high surface irregularity.

Declaration of Competing Interest

Acknowledgements

Appendix A. Supplementary material

Supplementary data to this article can be found online at https://doi.org/10.1016/j.jbiomech.2021.110445.

References

Altman, D.G., Bland, J.M., 1983. Measurement in medicine : the analysis of method comparison studies. Statistician 32, 307–317. https://doi.org/10.2307/2987937.

Bahaloo, H., Enns-Bray, W.S., Fleps, I., Ariza, O., Gilchrist, S., Soyka, R.W., Guy, P., Palsson, H., Ferguson, P.A., Helgason, B., 2018. On the failure initiation in the proximal human femur under simulated sideways fall. Ann. Biomed. Eng. 46, 270–283. https://doi.org/10.1007/s10439-017-1952-z.

Bayraktar, H.H., Morgan, E.F., Niebur, G.L., Morris, G.E., Wong, E.K., Keaveny, T.M., 2004. Comparison of the elastic and yield properties of human femoral trabecular and cortical bone tissue. J. Biomech. 37, 27–35. https://doi.org/10.1016/S0021-9290(03)00257-4.

Carter, D.R., Hayes, W.C., 1977. The compressive behavior of bone as a two-phase porous structure. J. Bone Jt. Surg. 59-A, 954–962. https://doi.org/10.1007/978-1-4471-5451-8_116.

Carter, D.R., Hayes, W.C., 1976. Bone compressive strength the influence of density and strain rate. Science (80-.) 194, 1174–1176. https://doi.org/10.1126/science.996549.

Dall'Ara, E., Luisier, B., Schmidt, R., Kainberger, F., Zysset, P., Pahr, D., 2013. A nonlinear QCT-based finite element model validation study for the human femur tested in two configurations in vitro. Bone 52, 27–38. https://doi.org/10.1016/j.bone.2012.09.006

Enns-Bray, W.S., Bahaloo, H., Fleps, I., Ariza, O., Gilchrist, S., Widmer, R., Guy, P., Pálsson, H., Ferguson, S.J., Cripton, P.A., Helgason, B., 2018. Material mapping strategy to improve the predicted response of the proximal femur to a sideways fall impact. J. Mech. Behav. Biomed. Mater. 78, 196–205. https://doi.org/10.1016/j.jmbbm.2017.10.033.

Gilchrist, S., Guy, P., Cripton, P.A., 2013. Development of an inertia-driven model of sideways fall for detailed study of femur fracture mechanics. J. Biomech. Eng. 135, https://doi.org/10.1115/1.4025390 121001.

Grassi, L., Isaksson, H., 2015. Extracting accurate strain measurements in bone mechanics: a critical review of current methods. J. Mech. Behav. Biomed. Mater. 50, 43–54. https://doi.org/doi:10.1016/j.jmbbm.2015.06.006

Grassi, L., Kok, J., Gustafsson, A., Zheng, Y., Väänänen, S.P., Jurvelin, J.S., Isaksson, H., 2020. Elucidating failure mechanisms in human femurs during a fall to the side using bilateral digital image correlation. J. Biomech. 106, 1–8. https://doi.org/10.1016/j.jbiomech.2020.109826.

Grassi, L., Schileo, E., Taddei, F., Zani, L., Juszczyk, M., Cristofolini, L., Viceconti, M., 2012. Accuracy of finite element predictions in sideways load configurations for the proximal human femur. J. Biomech. 45, 394–399. https://doi.org/10.1016/j.jbiomech.2011.10.019

Grassi, L., Väänänen, S.P., Amin Yavari, S., Weinans, H., Jurvelin, J.S., Zadpoor, A.A., Isaksson, H., 2013. Experimental validation of finite element model for proximal composite femur using optical measurements. J. Mech. Behav. Biomed. Mater. 21, 86–94. https://doi.org/10.1016/j.jmbbm.2013.02.006.

Grassi, L., Väänänen, S.P., Ristinmaa, M., Jurvelin, J.S., Isaksson, H., 2016. How accurately can subject-specific finite element models predict strains and strength of human femora? Investigation using full-field measurements. J. Biomech. 49, 802–806. https://doi.org/10.1016/j.jbiomech.2016.02.032.

Helgason, B., Gilchrist, S., Ariza, O., Vogt, P., Enns-Bray, W., Widmer, R.P., Fitze, T., Pálsson, H., Pauchard, Y., Guy, P., Ferguson, S.J., Cripton, P.A., 2016. The influence of the modulus-density relationship and the material mapping method on the simulated mechanical response of the proximal femur in side-ways fall loading configuration. Med. Eng. Phys. 38, 679–689. https://doi.org/10.1016/j.medengphy.2016.03.006.

Helgason, B., Gilchrist, S., Ariza, O., Chak, J.D., Zheng, G., Widmer, R.P., Ferguson, S.J., Guy, P., Cripton, P.A., 2014. Development of a balanced experimental-computational approach to understanding the mechanics of proximal femur fractures. Med. Eng. Phys. 36, 793–799. https://doi.org/10.1016/j.medengphy.2014.02.019.

Helgason, B., Taddei, F., Pálsson, H., Schileo, E., Cristofolini, L., Viceconti, M., Brynjólfsson, S., 2008. A modified method for assigning material properties to FE models of bones. Med. Eng. Phys. 30, 444–453. https://doi.org/10.1016/j.medengphy.2007.05.006.

Hernlund, E., Svedbom, A., Ivergård, M., Compston, J., Cooper, C., Stenmark, J., McCloskey, E.V., Jönsson, B., Kanis, J.A., 2013. Osteoporosis in the European Union: Medical management, epidemiology and economic burden: A report prepared in collaboration with the International Osteoporosis Foundation (IOF) and the European Federation of Pharmaceutical Industry Associations (EFPIA). Arch. Osteoporos. 8. https://doi.org/10.1007/s11657-013-0136-1.

Johannesdottir, F., Allaire, B., Bouxsein, M.L., 2018. Fracture prediction by computed tomography and finite element analysis: current and future perspectives. Curr. Osteoporos. Rep. 16, 411–422. https://doi.org/10.1007/s11914-018-0450-z.

Johannesdottir, F., Thrall, E., Muller, J., Keaveny, T.M., Kopperdahl, D.L., Bouxsein, M.L., 2017. Comparison of non-invasive assessments of strength of the proximal femur. Bone 105, 93–102. https://doi.org/10.1016/j.bone.2017.07.023.

Katz, Y., Yosibash, Z., 2020. New insights on the proximal femur biomechanics using Digital Image Correlation. J. Biomech. 101,. https://doi.org/10.1016/J.JBIOMECH.2020.109599 109599.

Keyak, J.H., Kaneko, T.S., Tehranzadeh, J., Skinner, H.B., 2005. Predicting proximal femoral strength using structural engineering models. Clin. Orthop. Relat. Res. 219–228. https://doi.org/10.1097/01.blo.0000164400.37905.22.

Koivumäki, J.E.M., Thevenot, J., Pulkkinen, P., Kuhn, V., Link, T.M., Eckstein, F., Jämsä, T., 2012. Ct-based finite element models can be used to estimate experimentally measured failure loads in the proximal femur. Bone 50, 824–829. https://doi.org/10.1016/j.bone.2012.01.012.

Morgan, E.F., Bayraktar, H.H., Keaveny, T.M., 2003. Trabecular bone modulus-density relationships depend on anatomic site. J. Biomech. 36, 897–904. https://doi.org/10.1016/S0021-9290(03)00071-X.

Orwoll, E.S., Marshall, L.M., Nielson, C.M., Cummings, S.R., Lapidus, J., Cauley, J.A., Ensrud, K., Lane, N., Hoffmann, P.R., Kopperdahl, D.L., Keaveny, T.M., 2009. Finite element analysis of the proximal femur and hip fracture risk in older men. J. Bone Miner. Res. 24, 475–483. https://doi.org/10.1359/jbmr.081201.

Parkkari, J., Kannus, P., Palvanen, M., Natri, A., Vainio, J., Aho, H., Vuori, I., Ja, M., 1999. Clinical Investigations Majority of Hip Fractures Occur as a Result of a Fall and Impact on the Greater Trochanter of the Femur: A Prospective Controlled Hip Fracture Study with 206 Consecutive Patients 183–187.

Pasco, J.A., Seeman, E., Henry, M.J., Merriman, E.N., Nicholson, G.C., Kotowicz, M.A., 2006. The population burden of fractures originates in women with osteopenia, not osteoporosis. Osteoporos. Int. 17, 1404–1409. https://doi.org/10.1007/s00198-006-0135-9.

Reilly, D.T., Burstein, A.H., 1975. The elastic and ultimate properties of compact bone tissue. J Biomech 8, 393–405. https://doi.org/10.1016/0021-9290(75)90075-5.

Reilly, D.T., Burstein, A.H., Frankel, V.H., 1974. The elastic modulus for bone. J. Biomech. 7. https://doi.org/10.1016/0021-9290(74)90018-9.

Schileo, E., Pitocchi, J., Falcinelli, C., Taddei, F., 2020. Cortical bone mapping improves finite element strain prediction accuracy at the proximal femur. Bone 136,. https://doi.org/10.1016/j.bone.2020.115348 115348.

Sutton, M.A., Orteu, J.-J., Schreier, H.W., 2009. Image Correlation for Shape, Motion and Deformation Measurements: Basic Concepts, Theory and Applications. Springer. https://doi.org/10.1007/978-0-387-78747-3_1.

Taddei, F., Schileo, E., Helgason, B., Cristofolini, L., Viceconti, M., 2007. The material mapping strategy influences the accuracy of CT-based finite element models of bones: An evaluation against experimental measurements. Med. Eng. Phys. 29, 973–979. https://doi.org/10.1016/j.medengphy.2006.10.014.

Viceconti, M., Qasim, M., Bhattacharya, P., Li, X., 2018. Correction to: Are CT-Based Finite Element Model Predictions of Femoral Bone Strength Clinically Useful?. Curr. Osteoporos. Rep. 1. https://doi.org/10.1007/s11914-018-0466-4.

Zysset, P.K., Dall'Ara, E., Varga, P., Pahr, D.H., 2013. Finite element analysis for prediction of bone strength. Bonekey Rep. 2, 1–9. https://doi.org/10.1038/bonekey.2013.120